Anharmonic Adsorption Free Energies and Apparent Activation Barriers for Mobile Reactants based on Molecular Dynamics Simulations

Philipp N. Plessow*

Institute of Catalysis Research and Technology, Karlsruhe Institute of Technology (KIT), Hermann-von-Helmholtz Platz 1, 76344 Eggenstein-Leopoldshafen, Germany

E-mail: plessow@kit.edu

Abstract

For zeolites, an approach is tested to compute adsorption free energies using molecular dynamics (MD) simulations based on density functional theory (DFT) at the PBE-D3 level of theory. The interaction free energy between zeolite and adsorbate is computed with Bennett's acceptance ratio method (BAR). An intermediate hard-sphere model is introduced to improve overlap between interacting and non-interacting system. Using this intermediate model also allows to alternatively evaluate the interaction reliably with both backward and forward free energy perturbation theory (FEPT). This approach works for weakly adsorbed systems and is applied to compute adsorption free energies of CO, propene and ketene at a surface methoxy species (SMS) in H-SSZ-13 at 200 °C and 400 °C. Intrinsic activation barriers for methylation of the adsorbed species are determined using constrained MD-simulations. Apparent activation free energies are then obtained as the sum of adsorption free energies and

the intrinsic activation barriers. The anharmonicity of the apparent activation free energies is negligible for CO and is in the range of -20 to -10 kJ/mol for propene and ketene. To address the limited accuracy of PBE-D3, calculations with the random phase approximation (RPA) are performed both as single points for stationary points and using FEPT based on the MD simulations. Both approaches agree to better than 5 kJ/mol and predict that PBE-D3 apparent activation barriers are too low by 20 to 30 kJ/mol.

Introduction

Zeolites are used in many industrial applications, for example as molecular sieves or as acidic catalysts.[1–5] Chemical reactions catalyzed by zeolites are routinely investigated with quantum chemical methods.[6–8] These investigations can give detailed insight into the chemical equilibrium and reaction kinetics. This can help to identify active species and reaction mechanism and, ultimately, to predict activities and selectivities of catalysts. The reliability of such an investigation will of course depend on the accuracy of the methods used. Usually, the Born-Oppenheimer approximation is used and there are then two decisive factors for the accuracy: 1) The precision of the electronic structure method and 2) The method used to describe the motion of the nuclei.

One common approach is based on a harmonic approximation of the potential energy surface (PES) around stationary points, such as minima and first-order saddle points. There are some advantages to this approach, for example that the stationary points and harmonic frequencies obtained from different simulations can be easily compared. Since this information requires only a very small amount of data, it can easily be provided and calculations are then very well defined and reproducible. If on the other hand, this data is not available, then different investigations on different local minima or saddle points can give differing results[9] that can then be difficult to explain. An additional advantage is that one can compute apparent activation free energies (see Fig. 1) directly, simply as the free energy difference

between transition state and clean zeolite and reactant in the gas phase. Furthermore, this approach is computationally inexpensive and corrections from a more advanced electronic structure method can be easily applied as single-point energy calculations. Partial optimization of the structure using higher level methods such as MP2 and extensions to treat anharmonic effects are also possible, but less common. Calculations of the type outlined above were pursued by Joachim Sauer and coworkers using accurate ab initio methods to get insights into the reactivity of zeolites.[10–14] The main disadvantage is that the description of a given state is limited to a single structure and, typically, the harmonic description of the PES in its vicinity. The harmonic approximation is expected to fail mainly, when a molecule or parts of it are relatively loosely bound and become more mobile than predicted by the harmonic approximation.

In the context of zeolites catalysis, reactants and products are often gas phase species, thus requiring adsorption and desorption steps. While gas phase species and the clean zeolite are expected to be described adequately by the harmonic approximation, this may not be the case for relatively weakly bound adsorbates. In the harmonic approximation, rotational and translational degrees of freedom present in gas phase molecules are lost upon adsorption and are converted into harmonic vibrations. Typically, this will lead to a loss in entropy and therefore an unfavorable contribution to the adsorption free energy. For loosely bound adsorbates, it is expected that this entropic penalty is overestimated with the harmonic approximation, resulting in too unfavorable adsorption free energies.

Molecular dynamics (MD) simulations are increasingly used to model the chemical reactivity of zeolites.[15] MD simulations are typically semiclassical: The nuclei are treated with classical mechanics based on forces obtained with a quantum mechanical method, such as DFT. The intrinsic lack of quantum effects of the nuclei, such as the zero point vibrational energy (ZPVE) is one of the limitations of this approach. The main advantage is that MD simulations are not limited to stationary points and the entire PES can be sampled, although this is in practice limited by the huge computational demand. As opposed to the harmonic

approximation, results of MD simulations are not as straightforward to compare or reproduce. It is technically possible to reproduce an MD simulation, when carefully initialized based on the initial structure, velocities and potentially the seed for a random number generator. Furthermore, well-converged MD simulations should give identical results, within the statistical uncertainty, irrespective of the initialization. In practice, the results of MD simulations can differ due to different electronic structure methods on top of possible convergence issues, which can be due to MD-specific setups (simulation time, time step, treatment of initiation period and thermostat). If the results of two MD simulations differ, it will be difficult to find the origin, even if both trajectories are available, which is not always the case due to their large size.

In zeolite catalysis, MD simulations are mainly carried out with GGA-functionals, due to the high computational demand of more accurate approaches. Usually, dispersion corrected PBE,[16] PBE-D3[17] or PBE-D2[18] is employed.

Improving the results of MD simulations with higher level methods is not straightforward and is rarely done, at least in the field of zeolite catalysis. This is also because most ab initio methods are only available for non-periodic systems. In previous work, we have attempted to improve the accuracy of MD-simulations by adding single-point corrections based on cluster models.[19] The more rigorous approach to this is using free energy perturbation theory (FEPT).[20] The main ab-initio method in use with a plane wave basis set and applicable to zeolites is the random phase approximation (RPA).[21–25] There are a few examples, where the RPA (or a RPA-trained machine learning model) has been applied to MD simulations on zeolites using FEPT.[26,26,27] Another approach is to fit a machine learning model to a higher level method such as the RPA and perform the MD directly using this model.[28] Many of these calculations would not be feasible without machine learning since direct application of RPA requires too much computing time.

Computing free energies with MD simulations is not straightforward, and in practice, only free energy differences between certain states are computed. For chemical reactions,

a couple of techniques were developed, which generally involve some reaction coordinate ξ, over which the reaction is driven and along which the change in free energy is computed. Techniques in use are metadynamics,[29] umbrella sampling or integration[30–32] and blue moon sampling.[33,34] As also discussed nicely in the recent review of van Speybroeck et al.,[15] all of these techniques have in common that they only work with all reactants co-adsorbed in the initial state. In practice, the adsorption and desorption steps necessary in zeolite catalysis are in most MD simulations not considered at all. This can be a serious limitation to such an investigation, if one wants to determine the reaction rates of a certain process. In many cases, at elevated temperatures, adsorption of reactants is unfavorable in terms of Gibbs free energy, see Fig. 1 for illustration. The apparent activation free energy will then be given relative to the reactant in the gas phase and will be higher than the intrinsic activation barrier. Simple estimates of the activity of a catalytic process as described by the energetic span model[35] would then require an apparent activation barrier. If data for adsorption is not available, as in many MD simulations, only the intrinsic activation barrier can be analyzed. Estimating the rate based only on the intrinsic barrier assumes that the coverage of the pre-adsorbed state is $\theta = 1$, which leads to an overestimation of the rate, if the coverage is actually much smaller, as in the example given in Fig. 1. This issue is furthermore enhanced by the fact that the commonly used PBE-D3 approach gives too low barriers. Both of these factors will thus add up to give too low barriers and too high rates. Mechanistic investigations that aim to explain experimentally observed reactions typically try to find a mechanism with low barriers. Employing methodology that gives systematically too low barriers may thus lead to a false positive evaluation of reaction mechanisms.

Anharmonic adsorption free energies in zeolites are rarely computed with DFT.[10,11,36] One approach explored recently, is to explicitly compute the anharmonicity of a given state using thermodynamic integration.[37] The anharmonic contribution to an adsorption free energy is then obtained as the difference of the anharmonicity of the adsorbed state, the clean zeolite and the molecule in the gas phase. An advantage of this approach is that it can also be

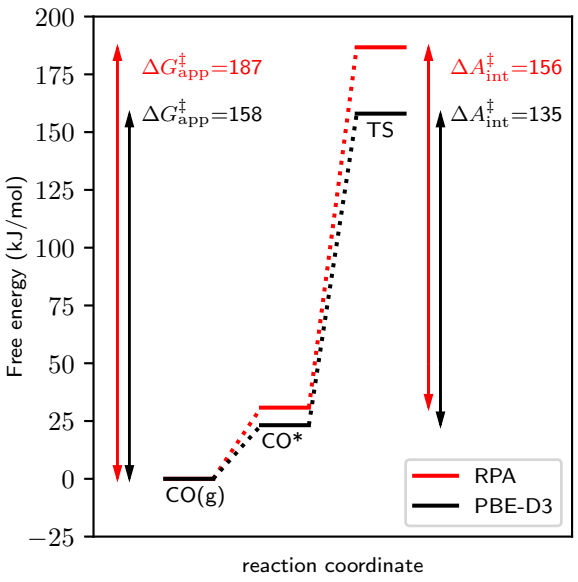

Figure 1: Example of a free energy profile illustrating intrinsic and apparent free energy for the case of CO-methylation at 400 °C.

applied directly to transition states.[38] The main technical challenge with this approach is that the harmonic approximation in Cartesian coordinates can be extremely bad for loosely bound adsorbates, complicating the thermodynamic integration. This can be improved by defining suitable intrinsic coordinates, which may nevertheless be challenging for specific systems.

Another approach to compute adsorption free energies is mainly used with force-fields based on Monte Carlo or MD simulations, also in related problems to study solvation, or binding to proteins.[39] Here, the interaction between the binding species (here zeolite and gas phase molecule) is switched on and the free energy difference is computed, typically with FEPT or the BAR method.[40] When using forward FEPT based on separate reactants this is also referred to as the Widom test particle method,[41–43,43–45] often used for pristine zeolites without acid sites. Generally, the free energy difference can only be computed reliably if the overlap between the states is sufficient. Similar to the approach followed here, in ref. 46 the Widom insertion method was used with DFT calculation on MOFs by partitioning the sampled space of the pore into three regions. In this way, rather than sampling all

space in the same way, the most densely populated areas can be sampled more efficiently. This can be expected to be the case when the adsorbate is very mobile, similar to the gas phase, but could be problematic for a strongly bound species. Recently, van Speybroeck and coworkers have employed machine-learned models including up to the CCSD(T) level of theory to perform grand canonical Monte Carlo simulations for the adsorption of water in MOFs.[47] One important aspect here is that machine learning allows to transfer a high level of accuracy to large and complex systems that could otherwise not be addressed directly with ab initio calculations.

In this work, we explore the calculation of adsorption free energies using MD simulations. We first discuss methodology and introduce an intermediate hard sphere model (IHSM) that can be used to improve overlap between the states. Using conventional blue moon (BM) calculations,[33] we then compute intrinsic free energy barriers. Together with the adsorption free energies, this provides apparent free energy barriers at the PBE-D3 level of theory. As relevant examples, we study the adsorption and methylation of CO, propene and ketene. Lastly, we use FEPT to compute the same quantities with RPA.

Methods

Computational Details of DFT calculations

All DFT calculations were performed with the Vienna Ab-Initio program package (VASP) in versions 6.3.0 and 6.4.3 using the projector augmented wave (PAW) method.[48,49] The standard PAW potentials were employed for all PBE[16] calculations along with real-space projectors. A cutoff of 400 eV was used for the expansion of the wave function in plane waves and a FFT-grid using lattice vectors with a norm up to 2 times larger than for the wave function, $|\mathbf{G}_{\text{cut}}|$ (PREC=Accurate) was used. For the bulk optimization of H-SSZ-13, an increased cutoff of 800 eV was used. The D3-correction was used in the zero-damping version.[17]

Stationary points were optimized with a convergence criterion of < 0.005 eV/Å and SCF convergence of 10^{-8} eV. Harmonic frequencies were computed based on a finite difference Hessian (central difference, offset 0.015 Å). The Hessian matrix was computed for the entire zeolite, but we also compare to the results with a partial Hessian including only the active site (Table S4). For comparison with MD simulations, we use the classical harmonic partition function[50] to obtain the free energy contribution:

$$A_{\text{harm.,class.}} = -\, k_B T \sum_i \ln\left(\frac{k_B T}{\hbar\omega_i}\right) \tag{1}$$

In Table S4, results using the partition sum for the quantum harmonic oscillator are also given, with negligible difference to the classical result. Symmetry is not considered in the rotational partition function, which makes a small difference for ketene with σ=2, see Table S4.

In MD simulations, the Andersen thermostat was employed together with a collision probability of 0.025 and a timestep of 0.5 fs for blue-moon calculations. For the calculation of adsorption properties, which do not depend on atomic masses, the mass of hydrogen was substituted with that of tritium (3.0 a.u.). Here a larger timestep (1 fs) and a corresponding collision probability of 0.05 was used. The initiation period for each MD simulation was determined using the Mann-Kendall test, based on the total energy averaged over blocks of 2000 steps.[51] After removing the initiation period, the correlation length was determined using the blocking method,[52] again based on the total energy.

RPA-calculations employ a cubic-scaling version[53] as implemented in VASP. All calculations were performed only at the Γ-point and use well-converged PBE wave functions. The standard RPA-calculations we used for FEPT were performed with a cutoff of 400 eV, standard PAW potentials and the settings prec=Normal and prec_fock=Normal. The type of structures as well as the precision (cutoff) that can be used with the RPA is limited by available RAM. For the single point calculations, we confirmed that using (prec=Accurate

and prec_fock=Accurate) settings leads only to negligible change (< 1 kJ/mol). The most demanding calculations we were still able to perform for the 12T-unit cell were with the GW PAW potentials using 500 eV with prec=Normal and prec_fock=Normal.

Adsorption free energies

We assume that the volume of the zeolite does not change upon adsorption of the adsorbate. Therefore, during adsorption at constant pressure, the pressure-volume work $w = pV_m = kT$ occurs. Consequently, the Gibbs free energy of adsorption ΔG_{ads} at a fixed pressure is:

$$\Delta G_{\text{ads}} = \Delta U_{\text{ads}} - T\Delta S_{\text{ads}} - kT. \tag{2}$$

The Helmholtz free energy of adsorption ΔA_{ads} at fixed volume does not include pressure-volume work. Therefore, it is identical to ΔG_{ads} at a reference pressure corresponding to the volume per molecule of the CHA-cell (806 Å^3), i.e. $p = 81$ bar at 200°C and $p = 115$ bar at 400°C. The reference pressure is adjusted to $p_0 = 1$ bar by adding $-k_B T \ln(p_0/p)$:

$$\Delta G_{\text{ads}} = \Delta A_{\text{ads}} - k_B T \ln\left(p_0/p\right). \tag{3}$$

The difference in Hamiltonians between the reference system, clean zeolite and adsorbate in the gas phase separated (sep) and the interacting system (int) is:

$$\Delta\mathcal{H} = \mathcal{H}_{\text{int}} - \mathcal{H}_{\text{sep}} \tag{4}$$

$$= V_{\text{int}}, \tag{5}$$

where V_{int} describes the interaction between zeolite and adsorbate. In the Widom test particle

method,[41–43] FEPT[20,39] is applied according to:

$$\Delta A = -k_B T \ln \left\langle \exp\left(-\frac{E_1 - E_0}{k_B T}\right) \right\rangle_0 \tag{6}$$

In practice, this is evaluated by running separate MD-simulations on zeolite and gas phase species and computing the interaction energies based on those trajectories. There are some issues with a straightforward application. First of all, within an MD simulation in VASP (or most programs), the movement of the center of mass is removed and therefore the adsorbate in the gas phase does not translate, as opposed to an actual gas phase moecule. To sample the interaction between zeolite and gas phase, we choose random positions of the adsorbate. This will result in the collision between adsorbate and zeolite in many instances, which one needs to take care of in some way. We use an intermediate hard-sphere model (IHSM), which removes this types of collisions. All simulations carried out can then be described with a general Hamiltonian:

$$\mathcal{H} = \mathcal{H}_{\text{sep}} + V, \tag{7}$$

where the Hamiltonian differs in the interacting potential V. For the non-interacting system, with the adsorbate in the gas phase, $V = 0$. For the fully interacting system, we have $V = V_{\text{int}}$ by definition (Eq. 5). The IHSM is defined as:

$$V_{\text{IHSM}} = \sum_{i=1}^{N_{\text{zeolite}}} \sum_{j=1}^{N_{\text{adsorbate}}} V_{\text{IHSM}}^{ij}(r_{ij}), \tag{8}$$

Here, r_{ij} are the pairwise atomic distances and the hard-sphere model uses pairwise radii r_{ij}^{hard} for each element combination (O-C, O-Si, etc.):

$$V_{\text{IHSM}}^{ij}(r_{ij}) = \begin{cases} 0 \text{ if } r_{ij} < r_{ij}^{\text{hard}} \\ \infty \text{ else} \end{cases} . \tag{9}$$

For simplicity, we enumerate the different states associated with the potentials:

$$V_0 = 0 \tag{10}$$

$$V_1 = V_{\mathrm{IHSM}} \tag{11}$$

$$V_2 = V_{\mathrm{int}} + V_{\mathrm{IHSM}} \tag{12}$$

$$V_3 = V_{\mathrm{int}} \tag{13}$$

The Helmholtz adsorption free energy is then computed as a sum of the differences between the intermediate models:

$$\Delta A_{\mathrm{ads}} = \Delta A_{1\text{-}0} + \Delta A_{2\text{-}1} + \Delta A_{3\text{-}2}. \tag{14}$$

The first term $A_{1\text{-}0}$ can be easily determined with FEPT at negligible numerical cost. Based on the separate MDs a certain number of paired adsorbate and clean zeolite structures is generated. We choose to extract every 5th MD-steps and to then simply pair the MD steps with the same iteration number, although any other combination would also work. For each adsorbate/zeolite pair, 100 random positions are chosen and the adsorbate is then added to the zeolite. Evaluation of the potential according to Eqs. 8 and 9 and FEPT (Eq. 6) is simple. The exponential is either 0 or 1 and the average of the exponential is thus equivalent to the fraction of adsorbate/zeolite pairs that do not collide according to the IHSM. This can be understood as a reduction of the accessible volume from that of the full unit cell v_0 to v_1:

$$\Delta A_{1\text{-}0} = -\, k_B T \, \ln \left\langle \exp\left(-\frac{V_{\mathrm{IHSM}}}{k_B T} \right) \right\rangle_0 \tag{15}$$

$$= -\, k_B T \, \ln \left(\frac{v_1}{v_0} \right) \tag{16}$$

The second contribution to the adsorption free energy, when evaluated with forward FEPT,

is:

$$\Delta A_{\text{2-1}}^{\text{FEPT-fw}} = -\, k_B T\, \ln \left\langle \exp\left(-\frac{V_{\text{int}}}{k_B T}\right) \right\rangle_1 . \tag{17}$$

The IHSM affects this calculation only indirectly by limiting the sampling to gas phase structures not colliding according to the hard spheres. The IHSM itself cancels in the potential difference $V_2 - V_1 = V_{\text{int}}$. Here the MD-simulation for state 1 is in practice again a combination of the simulation of separate gas phase and clean zeolite from which only pairs are created, which do not collide. The procedure for creating the structures is similar to that above for $\Delta A_{\text{1-0}}$, but due to the much higher computational cost, fewer structures are considered. As above, every 5th MD-step of the gas phase is used and paired with the corresponding MD-step of zeolite. A random position of the gas phase species is created until it does not collide with the zeolite and Eq. 17 is then evaluated with DFT single point energy calculations. One of the benefits of the IHSM is that backwards FEPT is also a good approximation:

$$\Delta A_{\text{2-1}}^{\text{FEPT-bw}} = -\, k_B T\, \ln \left\langle \exp\left(-\frac{V_{\text{int}}}{k_B T}\right) \right\rangle_2 . \tag{18}$$

Additionally, Bennett's acceptance ratio (BAR) method[54] can be applied, which is generally superior to one-sided FEPT. Here, both simulations of state 1 and state 2 are employed, when solving the following equation iteratively for parameter C:

$$\sum_{i=1}^{N_2} f(-V_{\text{int}}^i + C) = \sum_{i=1}^{N_1} f(V_{\text{int}}^i - C), \tag{19}$$

where on the left-hand side of the equation the sum runs over the N_2 structures in the employed trajectory of state 2 and on the right-hand side over the N_1 structures in the employed trajectory of state 1. The optimal switching function is the Fermi function (with

$\beta = k_B T$):

$$f(E) = \frac{1}{1 + \exp(\beta E)}. \tag{20}$$

The free energy difference is:

$$\Delta A_{2\text{-}1}^{\mathrm{BAR}} = C - k_B T \ln(N_2/N_1). \tag{21}$$

The variance $\sigma(\Delta A_{2\text{-}1}^{\mathrm{BAR}})$ is given by:[55]

$$\sigma(\Delta A_{2\text{-}1}^{\mathrm{BAR}}) = \frac{\langle f_2^2 \rangle / \langle f_2 \rangle^2 - 1}{\beta^2 \widetilde{N}_2} + \frac{\langle f_1^2 \rangle / \langle f_1 \rangle^2 - 1}{\beta^2 \widetilde{N}_1}. \tag{22}$$

Here, the number of structures N_1 and N_2 is reduced by the correlation length to the modified quantities $\widetilde{N}_1$ and $\widetilde{N}_2$. Furthermore, we use the shorthand notations $\langle f_1 \rangle^2$ and $\langle f_1^2 \rangle$ for the square of the average and the average of the square of the terms in the sum of the right-hand side of Eq. 19 and and analogously for state 2.

Bennett described his method[54] as similar to a Monte Carlo simulation, where, instead of changing the structure one instead changes the Hamiltonian. If the free energy difference is zero, then the probability to switch back and forth between the two Hamiltonians is equal. In Eq. 19, the energy difference is shifted by the parameter C, so that the overall probability to go from state 2 to state 1 and vice versa equals. If the lengths of the trajectories for state 1 and 2 are identical, C equals the free energy difference. If, not this is accounted for by the second term in Eq 21.

The third contribution is evaluated analogously to $\Delta A_{1\text{-}0}$:

$$\Delta A_{3\text{-}2} = + k_B T \, \ln \left\langle \exp\left(-\frac{V_{\mathrm{IHSM}}}{k_B T} \right) \right\rangle_3 . \tag{23}$$

As for $\Delta A_{1\text{-}0}$, the exponential is either 0 (n_0 times) or 1 (n_1 times) when averaging over

$n_0 + n_1$ structures and the free energy difference is then:

$$\Delta A_{3\text{-}2} = + k_B T \ln\left(\frac{n_1}{n_0 + n_1}\right). \tag{24}$$

As opposed to $\Delta A_{1\text{-}0}$, where the energy of the adsorbate in state 0 is in principle independent of its position and just part of the accessible volume is removed, this is different for $\Delta A_{3\text{-}2}$. For $\Delta A_{3\text{-}2}$, the energy depends on the position of the adsorbate in the cavity and the accessible volume removed by the IHSM is mainly at the edges of the cavity, where adsorbate and zeolite interact repulsively.

Results and Discussion

We use H-SSZ-13 as the catalyst due to its structural simplicity with only one T-site and because of the small size of its primitive cell with only twelve T-atoms. The structure of the clean surface methoxy species (SMS) is shown in Fig. 2 along with the indicated unit cell. The SMS was placed at the oxygen commonly labeled O4 that connects two T-atoms in the same double-six-ring, where one is in the upper and one in the lower six-ring. The unit cell was optimized for the pristine pure SiO_2-zeolite without symmetry constraints (lattice constants 9.35, 9.33 and 9.33 Å.) and subsequently kept fixed. Cartesian coordinates coordinate of stationary points are provided as SI.

Adsorption free energies and choice of hard-sphere radii

We will first discuss the choice of hard-sphere radii and how it influences the individual contributions to the adsorption free energy. We already want to make clear that the final value for the adsorption free energy is not very sensitive, when computed with either the BAR method or forward FEPT. However, when using backward FEPT, it is best to choose large radii.

The simplest estimate for hard sphere radii, based only on the simulations at hand,

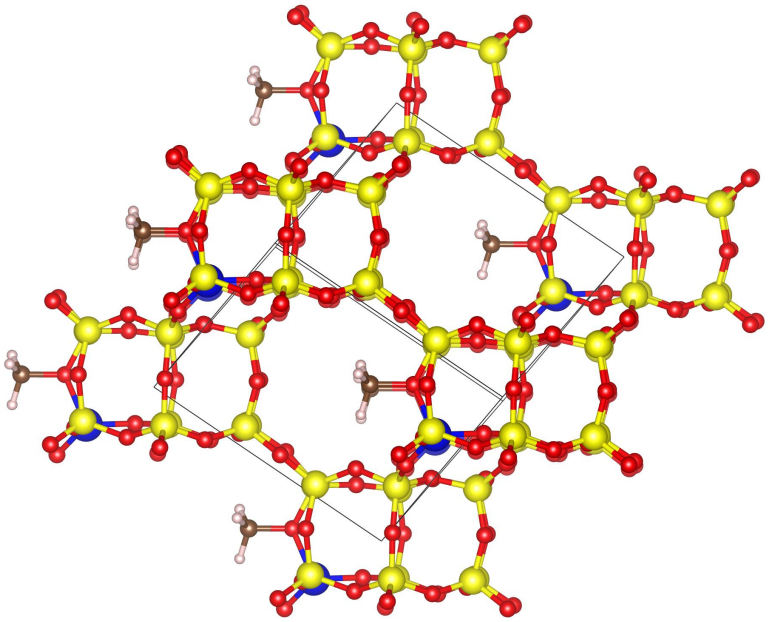

Figure 2: Structure of the H-SSZ-13 with an an SMS and the unit cell that includes 12T-sites indicated. Color code: Yellow: Si, blue: Al, red: O, black: H.

is obtained as the shortest pairwise distance observed during the MD simulation of the interacting MD. This is also the initial parametrization that we tested. It has the advantage of being well-defined and has the property that all structures sampled in the interacting MD do not collide according to the hard-sphere model, resulting in $\Delta A_{3\text{-}2} = 0$, see Table S1 in the SI. However, the disadvantage of using small hard-sphere radii is that this samples all of the repulsive interaction between adsorbate and zeolite in the interacting MD. This can be observed in Fig. 3a), which shows a histogram of the adsorption energy (more precisely $E_2 - E_1$). For both backward sampling based on the interacting MD and forward sampling based on the separate MD, the distribution shows a long, asymmetric tail towards positive, repulsive interaction. The average of the exponential factor required for FEPT is in practice computed as the mean value of a certain number of structures n, for example:

$$\left\langle \exp\left(-\frac{V_{\text{int}}}{k_B T}\right)\right\rangle = \frac{1}{n}\sum_{i=1}^{n} \exp\left(-\frac{E_2^{(i)} - E_1^{(i)}}{k_B T}\right). \tag{25}$$

In addition to Fig. 3a) for adsorption of ketene, we also show a histogram which is weighted by this exponential factor according to Eq. 25. As expected, for forward FEPT, the corresponding curve (dashed black) is slightly shifted to lower binding energies, see Fig. 3b). For backward FEPT, it is not only shifted to higher binding energies, but also shows strong contributions far away from the well-sampled area, see Fig. 3c). This makes backward FEPT with small radii very sensitive to the sampled structures. In practice, we have observed issues only for CO adsorbed at 400 °C, see Tables S1 and S2 and Fig S3 in the SI. Here backwards FEPT is dominated by only a handful out of thousands of structures, which are located in the repulsive, not very well sampled area. The results for backwards FEPT are off by 4.5 kJ/mol for this case.

The problem of backward FEPT being dominated by badly sampled repulsive interactions can be solved by simply using larger radii, see Figs. 3d), 3e) and 3f). The tail towards repulsive interaction is reduced significantly and along with that the contribution to backward

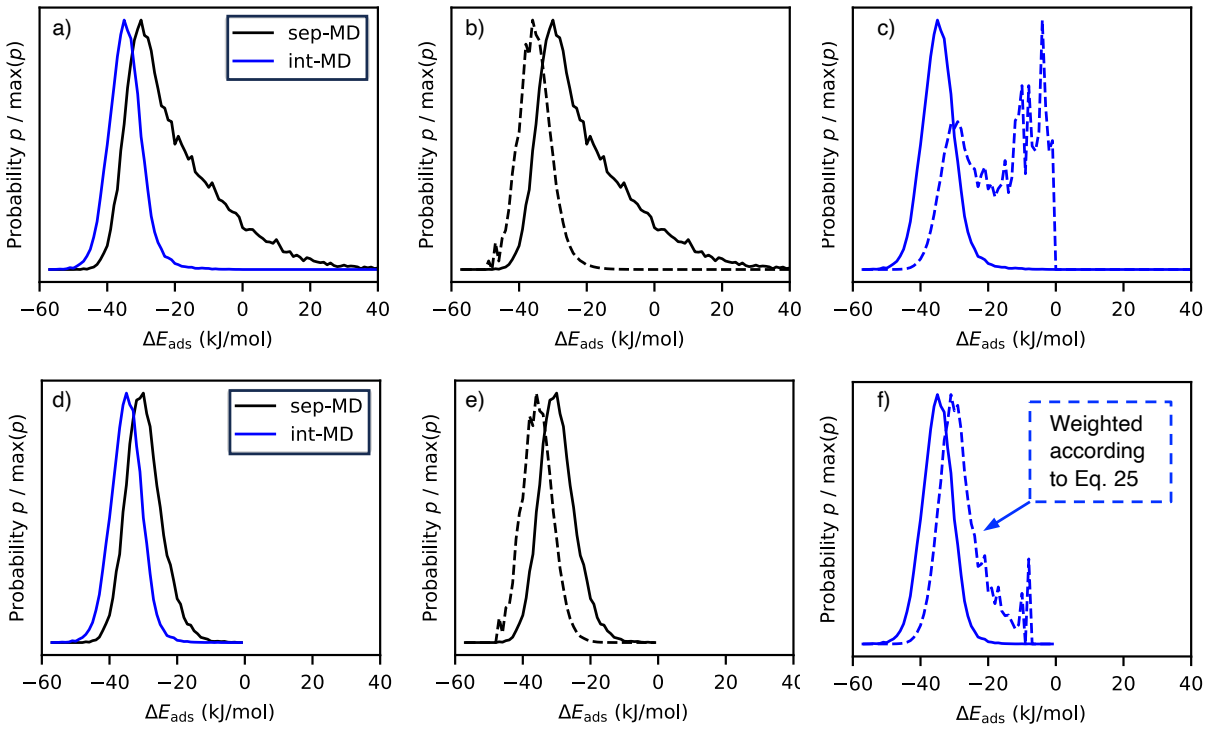

Figure 3: Overlap analysis for the adsorption of ketene at 400 °C. Histograms (bin size 0.01 eV) of the adsorption energy in presence of the IHSM, i.e. $\Delta E_{\text{ads}} = E_2 - E_1$. The smallest hard sphere radii are used in a-c) and the largest (Table 1) in d-f), note the difference in scale. a) and d) show the probability density based on interacting and separate MD. b) and e) show additionally the probability weighted with the Boltzmann factor, see Eq. 25. for the separate MD. c) and f) analogous to b) and e) but for the interacting MD.

FEPT from that region, see Fig. 3f). This can be easily tested at negligible computational cost, when analyzing the interacting MD by increasing the radii until the contributions in the badly sampled area shrink. The radii for CO happened to be particularly small. We have decided to present results here that use one set of radii, for simplicity. These parameters were obtained by using the largest radii for each pair observed in all simulations and by then increasing it by 10%, see Table 1. Additional results, showing the results with small radii specific to each MD (as discussed above), as well as results with these radii increased by 10% are shown in the SI. Overall, the final adsorption free energies obtained with the BAR methods differ at most by 0.2 kJ/mol when employing different radii. This difference lies within the variance σ, which is given in Table 2. When using the set of large radii, the largest deviation observed between forward and backward FEPT is 1 kJ/mol.

Can the hard sphere radii be chosen too large? Increasing the radii reduces the part of the interacting MD that does not violate the hard-sphere parameters and remains useful to compute $\Delta A_{2\text{-}1}$ and thus worsens the sampling. In practice, even using the largest radii, only 10% of the interacting MD violates the hard-sphere model.

Table 1: Maximum pairwise distances between adsorbate and zeolite adsorbed during the MD of the interacting system in Å. The column labeled 'max' list the maximum values, increased by 10%, which were used to compute the results in the main text.

	CO		propene		ketene		
T(°C)	200	400	200	400	200	400	
pair							max
Al-C	3.0	2.7	3.1	3.0	3.0	3.2	3.5
Al-H	-	-	2.4	2.2	2.6	2.5	2.8
Al-O	2.9	3.0	-	-	2.8	2.3	3.3
C-C	2.7	2.6	2.7	2.8	2.9	2.8	3.2
C-H	2.0	1.9	2.0	2.0	2.1	2.0	2.3
C-O	2.5	2.4	2.7	2.6	2.6	2.4	2.9
C-Si	2.9	2.8	3.2	3.2	3.2	3.0	3.5
H-H	-	-	1.4	1.4	1.6	1.5	1.8
H-O	2.0	1.9	1.9	1.8	1.7	1.6	2.2
H-Si	-	-	2.4	2.3	2.5	2.3	2.7
O-O	2.4	2.4	-	-	2.4	2.3	2.7
O-Si	2.8	2.8	-	-	2.9	2.8	3.1

Table 2 shows the computed contributions to ΔA_{ads}. The main contributions are the decrease in volume leading to $\Delta A_{1\text{-}0} > 0$ and the actual binding leading to $\Delta A_{2\text{-}1} < 0$. The absolute contribution of $\Delta A_{3\text{-}2} < 0$ is less than one kJ/mol. It can furthermore be seen that the actual binding contribution $\Delta A_{2\text{-}1}$ depends only very weakly on temperature, with differences (BAR) below 1 kJ/mol.

Besides the discussed issues for CO at 400 °C, the results with the different set of radii (Tables S1 and S2) differ in an expected way, shifting contributions between $\Delta A_{1\text{-}0}$, $\Delta A_{2\text{-}1}$ and $\Delta A_{3\text{-}2}$ while the overall result for ΔA_{ads} changes little. The smaller the radii, the smaller are the absolute values of $\Delta A_{1\text{-}0}$ and $\Delta A_{3\text{-}2}$. Using the smallest radii, by definition, gives $\Delta A_{3\text{-}2}$=0. Adjusting the reference pressure to 1 bar using Eq. 3, we obtain the Gibbs free energies of adsorption, can also be compared to the those obtained with the harmonic approximation. As expected, the harmonic approximation leads to too weak binding, with deviations ranging from 10 to 20 kJ/mol.

Table 2: Contributions to adsorption free energies computed at the PBE-D3 level of theory in kJ/mol. A reference pressure of 1 bar is used for ΔG_{ads}.

		CO		propene		ketene	
	T(°C)	200	400	200	400	200	400
quantity	method						
$\Delta A_{1\text{-}0}$	MD	10.5	15.1	16.2	23.3	14.0	19.7
$\Delta A_{2\text{-}1}$ FEPT-bw	MD	-17.8	-17.6	-43.5	-43.9	-31.8	-31.7
$\Delta A_{2\text{-}1}$ BAR	MD	-17.8	-17.6	-43.9	-43.7	-32.4	-31.9
$\sigma(\Delta A_{2\text{-}1}$ BAR)	MD	0.1	0.1	0.2	0.2	0.2	0.2
$\Delta A_{2\text{-}1}$ FEPT-fw	MD	-17.9	-17.7	-44.5	-43.7	-32.9	-32.2
$\Delta A_{3\text{-}2}$	MD	-0.5	-0.8	-0.3	-0.6	-0.4	-0.8
ΔA_{ads}	MD	-7.8	-3.4	-27.9	-21.0	-18.8	-13.0
$-k_B T \ln(p_0/p)$	MD	17.3	26.6	17.3	26.6	17.3	26.6
ΔG_{ads}	MD	9.5	23.2	-10.7	5.6	-1.5	13.6
ΔG_{ads}	harm	20.8	37.5	4.5	25.7	15.1	35.8
$\Delta\Delta G_{\text{ads}}$	anharm	-11.3	-14.3	-15.2	-20.1	-16.6	-22.2

Activation barriers

Intrinsic activation free energies were computed using the usual blue moon (BM) sampling approach using constrained MD simulations as implemented in VASP. All methylations can be described with a typical reaction coordinate for an S_N2-reaction:

$$\xi = d_2(\mathrm{O_{zeolite}} - \mathrm{C_{methyl}}) - d_1(\mathrm{C_{reactant}} - \mathrm{C_{methyl}}). \tag{26}$$

Here, two bond distances are involved: reactant carbon to the carbon of the methyl group (d_1) and the zeolite oxygen to the carbon of the methyl group (d_2). This is also illustrated in Fig. 4a). Constrained simulations with a length of about 90 ps (180,000 steps) were carried out for different values of ξ (16 for CO, 14 for propene and and 14 for ketene).

We did not investigate the products of the methylation reaction, which are in most cases known, even if some discussions have been concerned with what exactly happens after the transition state. CO-methylation yields a protonated ketene (acylium cation), which may subsequently be deprotonated by the zeolite to the ketene, or could coordinate to the zeolite to form a surface acetyl species. The barriers for rearrangement between these species are low, so that the question, which forms first is of no immediate consequence. Ketene methylation leads to analogous species with one hydrogen atoms substituted by a methyl group. Propene methylation is more complicated. Potential neutral product molecules are 1-butene, n-butene, iso butene and methyl cyclopropane. Bell and coworkers have investigated direct propene methylation by methanol (rather than stepwise by SMS) at 623 K in MFI using both static approaches and quasiclassical trajectories and have concluded that the main product is n-butene, in agreement with the experimental investigations.[56] They found that the reaction proceeds via an intermediate methylcyclopropane (mPCP+) carbocation, which quickly rearranges to the 2-butyl cation, which is more stable and may exists for more than 1 ps before giving the final product. In our constrained MD simulations, for values of the reaction coordinate at or after the TS ($\xi \geq$ -0.26 Å), the barrier for rearrangement to

the tert-butyl cation is accessible. The chosen constraint (Eq. 26) does not prevent that the methyl group attaches to the central carbon of propene and it turns out that starting from the constrained state, the barrier for rearrangement to the tert-butyl cation is low enough to be overcome. Rearrangement to the tert-butyl cation is irreversible due a large gain in energy and is easily identified by the distance between methyl group and the central carbon of propene, which is > 2.4 Å in the TS and < 1.7 Å in the tert-butyl cation. For the analysis of the constrained MD at $\xi^{\ddagger}$ = -0.26 Å, we have only kept the ≈40 ps before rearrangement. Additionally, rearrangement can be prevented with a Fermi bias potential, which we placed at a value of the mentioned C-C distance of 2.0 Å, with a height of 1 eV and a width defined in VASP with FBIAS_D=150. Using this additional constraint, more simulations were performed at $\xi^{\ddagger}$ = -0.26 Å, giving very similar free energy gradients close to zero (absolute values with and without constraint < 0.01 eV/Å), which were eventually not used in the analysis. For the point at $\xi = 0.2$ Å after the TS used for propene (see SI), only the MDs including the described bias potential were performed and analyzed. In the end, we expect the influence of the additional constraint after the TS and of the rearrangement itself to be small. The contribution to $\Delta A^{\ddagger}_{\text{int}}$ stemming from integration of the free energy gradient in the affected range of ξ from -0.4 to -0.26 Å is only 1.6 kJ/mol, since the free energy gradient is of course very small close to the TS. Furthermore, we observe in all cases here, that the free energy gradient changes almost linearly in the TS region (Fig. 4b), which is also the case for propene.

Conditional averages at a given value of ξ of some quantity O in the blue moon ensemble are obtained as:[33]

$$\langle O \rangle_{\xi} = \frac{\langle Z^{-1/2} O(\xi) \rangle_{\xi}}{\langle Z^{-1/2} \rangle_{\xi}}, \tag{27}$$

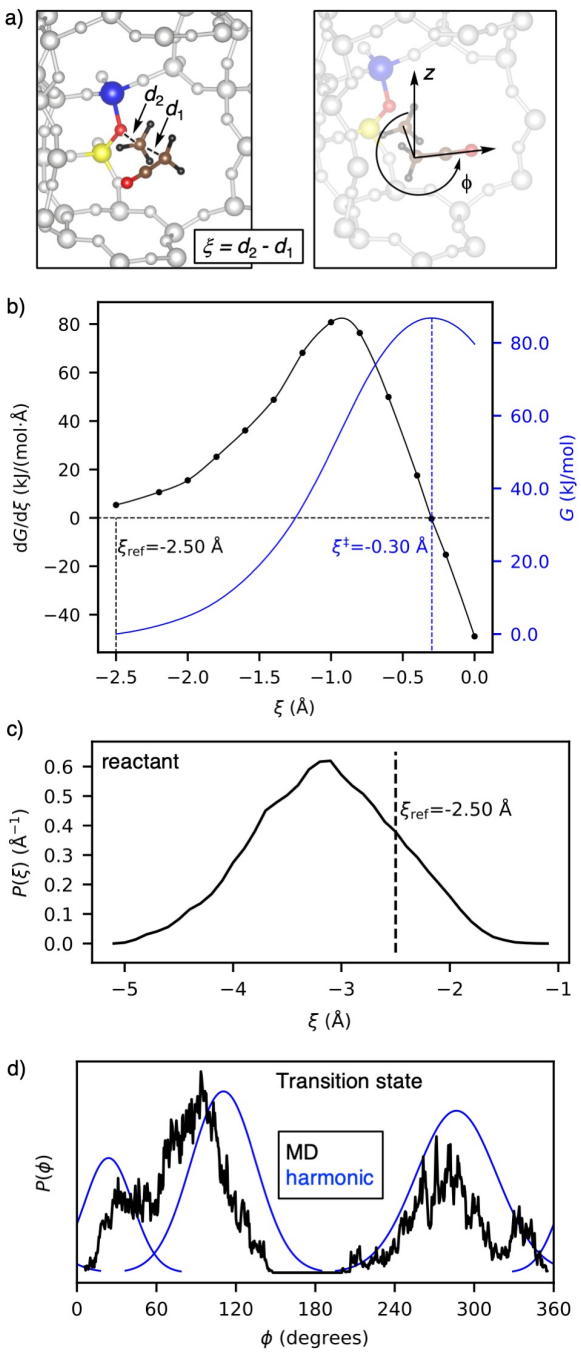

Figure 4: Activation barrier computed for ketene methylation at 400 °C using blue-moon sampling. a) Illustration of the employed reaction coordinates. b) Obtained free energy gradient and free energy profile. The position of the transition state ($\xi^{‡}$) and the choice for initial state (ξ_{ref}) is indicated. c) Histogram of the probability density for the reaction coordinate obtained for the unconstrained initial state. d) Histogram of the probability density for the torsional angle ϕ at $\xi = \xi^{‡}$.

with the Z as the inverse of the mass metric tensor:

$$Z = \sum_{i=1}^{3N} \frac{1}{m_i} \left(\frac{\partial \xi}{\partial q_i} \right)^2 . \tag{28}$$

Here, N is the number of atoms and q_i are the atomic coordinates. The free energy gradient is:[34]

$$\left. \frac{\partial A}{\partial \xi_k} \right|_{\xi} = \frac{\langle Z^{-1/2} Y(\xi) \rangle_{\xi}}{\langle Z^{-1/2} \rangle_{\xi}}, \tag{29}$$

with

$$Y(\xi) = \left[-\lambda + \frac{k_B T}{Z} \sum_{i=1}^{3N} \frac{1}{m_i} \frac{\partial \xi}{\partial q_i} \frac{\partial Z}{\partial q_i} \right], \tag{30}$$

where the Lagrangian Multiplier (λ) comes from the SHAKE algorithm.[57] The free gradient was determined for each value of ξ, see also Table S8.

The free energy gradient can then be integrated between a reference value of the reaction coordinate ξ_{ref} and the value at the transition state $\xi^{\ddagger}$:

$$A(\xi^{\ddagger}) - A(\xi_{\text{ref}}) = \int_{\xi_{\text{ref}}}^{\xi^{\ddagger}} \mathrm{d}\xi \left. \frac{\partial A}{\partial \xi_k} \right|_{\xi} . \tag{31}$$

We performed this integration based on a spline-interpolation of the computed values of free energy gradient. The variance of the free energy difference in Eq. 31 is obtained by integrating the squared variance (given in Table S8) in the same way. An Akima-spline was used, but very similar (difference < 0.1 kJ/mol) results were obtained for different spline interpolations (natural spline or smoothed not-a-knot spline). The results are listed in Table 3. Notably, Eq. 31 is not the activation barrier suitable for calculating reaction rate constants based on transition state theory or for comparison with the harmonic approximation.[58]

Instead, the intrinsic free energy barrier is obtained as:

$$\begin{aligned}\Delta A^{\ddagger}_{\mathrm{int}} =& A(\xi^{\ddagger}) - A(\xi_{\mathrm{ref}}) \\ & - k_B T \ln\left[\frac{h}{k_B T}\frac{\langle\dot{\xi}\rangle_{\xi^{\ddagger}}}{2} P(\xi_{\mathrm{ref}})\right].\end{aligned} \tag{32}$$

We note that a free energy barrier based on metadynamics[29] or umbrella integration[30–32] is obtained in the same way. In Table 3, the last term in Eq. 32 is split into two parts:

$$\begin{aligned}-k_B T \ln\left[\frac{h}{k_B T}\frac{\langle\dot{\xi}\rangle}{2} P(\xi_{\mathrm{ref}})\right] =& - k_B T \ln\left(\frac{h}{k_B T}\frac{\langle\dot{\xi}\rangle}{2\,\xi_0}\right) \\ & - k_B T \ln(P(\xi_{\mathrm{ref}}) \cdot \xi_0).\end{aligned} \tag{33}$$

Here, $P(\xi_{\mathrm{ref}})$ is the probability distribution of the unconstrained initial state evaluated at the ξ_{ref}. The quantity ξ_0 on the right hand side is introduced to make the argument of the natural logarithm unitless, here we use $\xi_0 = 1$ Å. The velocity term $\langle\dot{\xi}\rangle$ is computed as:

$$\langle\dot{\xi}\rangle_{\xi^{\ddagger}} = \sqrt{\frac{2k_B T}{\pi}}\frac{1}{\langle Z^{-1/2}\rangle_{\xi^{\ddagger}}} \tag{34}$$

Table 3 lists the contributions from BM-calculations as described above. We have used ξ_{ref} = -2.5 Å, because this value is close enough to the reactant state to allow reliable evaluation of $P(\xi_{\mathrm{ref}})$ through the histogram approximation, see Fig. 4c). The location of the transition state does not vary much with temperature ($\leq$ 0.01 Å) and is similar for propene and ketene ($\approx$ -0.30 Å). For CO, the transition state occurs later ($\approx$ 0.06 Å), in line with the higher barrier. The contributions according to Eq. 33 are similar for the different species and add up to 5-10 kJ/mol, generally increasing the barrier.

For comparison, harmonic intrinsic activation barriers are also listed in Table 3, as well as the anharmonicity, which is simply the difference between the MD (blue moon) and the harmonic result. The intrinsic barrier is usually somewhat lower ($<$ 10 kJ/mol) in

Table 3: Contributions to activation free energies obtained with PBE-D3 using blue-moon sampling ('MD') for all studied reactions. Results obtained with the harmonic approximation ('harm') are also shown. Additionally, the anharmonic part ('anharm') defined as the difference between 'MD' and 'harm' is listed. Additionally, apparent Gibs free energies of activation are listed. These are simply the sum of $\Delta A^{\ddagger}_{\mathrm{int}}$ and ΔG_{ads}. All free energy contributions are given in kJ/mol, $\xi^{\ddagger}$ and ξ_{ref} in Å. Gibbs free energies use a reference pressure of 1 bar for gas phase species.

		CO		propene		ketene	
	T(°C)	200	400	200	400	200	400
quantity	method						
$\xi^{\ddagger}$	MD	0.06	0.06	-0.25	-0.26	-0.30	-0.30
ξ_{ref}	MD	-2.50	-2.50	-2.50	-2.50	-2.50	-2.50
$A(\xi^{\ddagger}) - A(\xi_{\mathrm{ref}})$	MD	117.8	124.8	85.3	87.6	81.5	86.8
$-k_B T \ln\left(\frac{h}{k_B T}\frac{\langle\dot{\xi}\rangle_{\xi^{\ddagger}}}{2\text{Å}}\right)$	MD	2.3	4.3	2.3	4.3	2.3	4.3
$-k_B T \ln(P(\xi_{\mathrm{ref}}) \cdot \text{Å})$	MD	3.1	5.7	2.4	4.1	3.9	5.4
$\Delta A^{\ddagger}_{\mathrm{int}}$	MD	123.1	134.8	90.0	96.0	87.7	96.6
$\sigma(\Delta A^{\ddagger}_{\mathrm{int}})$	MD	1.0	1.3	1.2	1.4	1.1	1.2
$\Delta A^{\ddagger}_{\mathrm{int}}$	harm	114.3	122.2	87.4	94.2	79.3	87.2
$\Delta\Delta A^{\ddagger}_{\mathrm{int}}$	anharm	8.8	12.6	2.6	1.7	8.4	9.4
$\Delta G^{\ddagger}_{\mathrm{app}}$	MD	132.7	158.0	79.3	101.5	86.2	110.1
$\Delta G^{\ddagger}_{\mathrm{app}}$	harm	135.1	159.7	91.9	119.9	94.4	123.0
$\Delta\Delta G^{\ddagger}_{\mathrm{app}}$	anharm	-2.5	-1.7	-12.5	-18.4	-8.2	-12.8

the harmonic approximation. This is because the initial state (adsorbed reactant) is more anharmonic than the transition state.

Apparent activation free energies are computed simply as:

$$\Delta G^{\ddagger}_{\mathrm{app}} = \Delta A^{\ddagger}_{\mathrm{int}} + \Delta G_{\mathrm{ads}}. \tag{35}$$

Together with the adsorption free energies from Table 2, we thus obtain the values for $\Delta G^{\ddagger}_{\mathrm{app}}$ given in Table 3. For the apparent activation barriers, all anharmonicities are negative. The effect for CO is small (about -3 kJ/mol), but more significant for propene and ketene (-20 to -10 kJ/mol).

The difference between free energies obtained using the harmonic classical and quantum partition functions are generally small, in the range of 2 kJ/mol or less (Table S4). An additional correction arises in the quantum version of the rotational partition function of ketene with a symmetry number of $\sigma = 2$, which has not been considered in the main text. Considering the correct symmetry number shifts the free energy of ketene in the gas phase up by 3 to 4 kJ/mol, thus lowering ΔG_{ads} and $\Delta G^{\ddagger}_{\mathrm{app}}$ by the same amount (see Table S4).

The origin of anharmonicity is clear for the adsorbed reactant state. In the MD simulation, the adsorbed reactants rotate and translate in the pore, while they only perform soft vibrations in the harmonic approximation. The harmonic approximation is thus qualitatively and quantitatively inadequate. We would also like to point out that no attempt has been made to find the global minimum for the reactant state. Instead, the minimum obtained by displacing the transition state along the reaction mode and optimizing towards the endpoints has been used.

For the transition state, the origin of anharmonicity is less obvious. One clear contribution is the hindered rotation of the reactant along the CH_3-C axis (bond distance d_1) along which methylation occurs. For CO, no such rotation occurs, in line with the observed negligible anharmonicity for $\Delta G^{\ddagger}_{\mathrm{app}}$. For ketene, a histogram of the torsional angle during the MD

simulation is shown in Fig. 4d). which clearly shows an anharmonic behavior. The angle ϕ is given relative to the most upright position of ketene, i.e. relative to the z-axis from which the component parallel to CH_3-C vector is removed. Three distinct saddle points were obtained for ketene methylation, with torsional angles of ($\phi = 111°$, 24°, 287°). These saddle points are, depending on temperature, quite close in Gibbs free energy, generally within 5.5 kJ/mol. Truhlar and coworkers have proposed methods to compute activation free energy based on multiple conformers.[59] We did not pursue such advanced approaches to improve upon the harmonic approximation based on a single structure. It is also noteworthy that the rotation of the reactant (ketene or propene) is coupled to tilting of the SMS and is hindered by the zeolite framework. Therefore, no smooth relaxed potential energy surface is obtained, as one might expect for more benign torsional modes in gas phase molecules. The first step to include multiple conformers in the transition state is to simply add the harmonic partition functions,[59] which is expected to fail if the distributions of the different harmonic wells overlap significantly. In Table S7, combining two or three out of the three conformers for the transition state of ketene is tested, giving a stabilization of up to 5.2 kJ/mol over the description of using just the most stable single conformer. For propene, the situation is similar, with two conformers of the transition state, leading to a stabilization of up to 3.5 kJ/mol if both are considered.

Besides the intrinsic accuracy of the harmonic approximation, there are a couple of factors limiting the achieved precision in practice. First of all, if the most stable saddle points has not been located, the transition state free energy will be overestimated. This would result in an overestimation of the barrier, unless a similar issue exists for the initial state, in which case the barrier could be off in any direction. Secondly, there are a number of factors limiting the precision of the harmonic frequencies, which are in plane wave DFT typically evaluated numerically based on the Hellmann-Feynman forces. These limiting factors are the geometric convergence of the stationary points, SCF convergence and the procedure to obtain the numerical Hessian, here two-point central difference with an offset of 0.015 Å.

An additional limiting factors in the electronic structure method for plane wave codes is the density cutoff, in VASP typically changed via prec = Normal/Accurate. Given the numerical calculation of the Hessian, it is common practice in computational catalysis to compute only partial Hessians, where typically only the adsorbate and the active site is included. Results using a partial Hessian (Si-O(CH_3)-Al and adsorbate) are given in Table S4 and deviate up to about 10 kJ/mol. Importantly, in the investigated cases, the error of using only partial Hessians always makes adsorption weaker and barriers higher and therefore systematically increases the intrinsic errors of the harmonic approximation. It is well-known that numerical inaccuracies can lead to noisy frequencies. Sloppy convergence criteria combined with soft modes can lead to too low or even negative curvature, resulting in too low or even imaginary harmonic frequencies. The most rigorous way of dealing with this is to generally apply stricter criteria and to re-optimize minima which are actually saddle points after distorting along the undesired negative curvature modes. Another common approach to deal with this issue is to instead replace all frequencies that are imaginary or fall below a certain threshold with this threshold. Typical values in heterogeneous catalysis are 10 or 12 cm^{-1}, which we have also employed in previous work. We usually we find no frequencies falling in this range, also because weakly bound states are often not explicitly computed. Here we have one case, the lowest frequency for adsorbed propene is 7 cm^{-1} and was shifted to 12 cm^{-1}. Again, we point out that no attempt has been made to find a more stable minimum for the adsorbed structure. Other typical shift-values in use mainly for calculations in solution are 60 or even 100 cm^{-1}, which are motivated by the fact that large-amplitude vibrations may be hindered by solvent molecules. Clearly this is not the case here and the lowest-frequency vibrational modes encountered in the transition states (20 to 40 cm^{-1}) are significant. We have tested using a minimum frequency of 100 cm^{-1} (table S4), which increases harmonic apparent barriers by 10 to 20 kJ/mol, further worsening the agreement with MD-simulations.

RPA free energies

For the harmonic approximation, RPA-energies were computed simply as single points at the stationary points. For the MD-simulations, FEPT was performed using every 1000th MD-step (safely above the correlation length), which gives a total free energy difference $\Delta A_{\mathrm{FEPT/MD}}$(RPA-PBE-D3) for each state (given in Table S10). We furthermore used FEPT in the second-order cumulant expansion version, with ΔE as the energy difference between PBE-D3 and RPA for a given MD step:

$$\Delta A_{\mathrm{FEPT/MD}}(\text{RPA-PBE-D3}) = \langle \Delta E \rangle - \frac{\beta}{2} \langle [\Delta E - \langle \Delta E \rangle]^2 \rangle. \tag{36}$$

The second-order cumulant expansion of FEPT was used due to the small number of structures (100 to 200), but reaction free energies using the full exponential expression (Eq. 6) differ at most by 1.3 kJ/mol, see Table S11. Total RPA free energies are calculated as:

$$A_{\mathrm{FEPT/MD}}(\text{RPA}) = \Delta A_{\mathrm{FEPT/MD}}(\text{RPA-PBE-D3}) + A_{\mathrm{MD}}(\text{PBE-D3}). \tag{37}$$

Reaction and activation free energies at the RPA-level are then obtained simply as differences of the free energies of the involved states based on Eqs. 36 and 37. The FEPT-correction to the intrinsic activation barrier (Eq. 32) is obtained in the same way, as described and derived in ref. 60. Table 4 lists the results of the RPA calculations. Furthermore the results of different levels of theory are shown in Fig. 5. The FEPT values for each state are listed in Table S10, which also gives the respective I_{w}-index.[60] The value of I_{w}-index is generally in the range of 0.10 to 0.30 thus indicating that a reasonable number of structures contribute to FEPT, which can thus be considered reliable. As expected, RPA gives weaker adsorption energies and higher barriers than PBE-D3. In our recent work[61] we tested RPA/cc-pVQZ on large 46T-cluster models of H-SSZ-13. For $\Delta G^{\ddagger}_{\mathrm{app}}$, we found that RPA/cc-pVQZ gives barriers that are about 5 kJ/mol too high for CO and about 5 kJ/mol too low for both

propene and ketene. As opposed to the plane wave calculations herein, these RPA/cc-pVQZ contain some amount of basis set super position error (BSSE) and are therefore expected to be lower than the complete basis set limit. Overall, we thus expect the RPA to be accurate for the barriers investigated in this work. For CO, $\Delta A^{\ddagger}_{\mathrm{int}}$ is higher with RPA compared to PBE-D3 by 20 kJ/mol, while it is only about 10 kJ/mol for ketene and propene. Together with the weaker binding, this gives for $\Delta G^{\ddagger}_{\mathrm{app}}$ barriers which are higher by about 25 kJ/mol for ketene and 30 kJ/mol for both CO and propene.

Table 4: Results of RPA calculations in kJ/mol for 200 °C and 400 °C. The obtained differences in free energies relative to PBE-D3 (RPA-PBE-D3) are labeled $\Delta\Delta G$ and $\Delta\Delta A$ for adsorption and intrinsic and apparent activation barriers. Additionally, the RPA value for ΔG and ΔA is given for the MD simulations, which is obtained by adding the MD (FEPT) result obtained here to the MD results given in Tables 2 and 3. Gibbs free energies use a reference pressure of 1 bar for gas phase species.

		CO		propene		ketene	
	T(°C)	200	400	200	400	200	400
quantity	method						
$\Delta\Delta G_{\mathrm{ads}}$	FEPT/MD	8.7	7.6	17.0	19.1	12.5	12.5
$\Delta\Delta G_{\mathrm{ads}}$	SP	10.1		20.5		15.6	
$\Delta\Delta G_{\mathrm{ads}}$	SP/500eV	8.6		19.1		12.4	
$\Delta\Delta A^{\ddagger}_{\mathrm{int}}$	FEPT/MD	21.7	21.1	11.2	9.2	11.9	9.8
$\Delta\Delta A^{\ddagger}_{\mathrm{int}}$	SP	18.4		10.1		9.9	
$\Delta\Delta A^{\ddagger}_{\mathrm{int}}$	SP/500eV	22.4		12.8		13.3	
$\Delta\Delta G^{\ddagger}_{\mathrm{app}}$	FEPT/MD	30.4	28.7	28.2	28.3	24.4	22.4
$\Delta\Delta G^{\ddagger}_{\mathrm{app}}$	SP	28.5		30.6		25.6	
$\Delta\Delta G^{\ddagger}_{\mathrm{app}}$	SP/500eV	31.0		32.0		25.7	
ΔG_{ads}	FEPT/MD	18.2	30.8	6.4	24.6	11.0	26.1
$\Delta A^{\ddagger}_{\mathrm{int}}$	FEPT/MD	144.8	155.9	101.2	105.2	99.6	106.4
$\Delta G^{\ddagger}_{\mathrm{app}}$	FEPT/MD	163.1	186.7	107.6	129.8	110.6	132.5

If we compare the difference between RPA and PBE-D3 evaluated as a single point (SP) and with FEPT, we find that they differ at most by 3.5 kJ/mol and on average by 2.0 kJ/mol. This is on the same order of magnitude as the difference between RPA evaluated with standard PAW potentials and 400 eV cutoff and RPA evaluated with GW PAW potentials and 500 eV cutoff. In this case, the inaccuracy introduced by computing the difference between PBE-D3 and RPA using only a single point is therefore within the precision of a

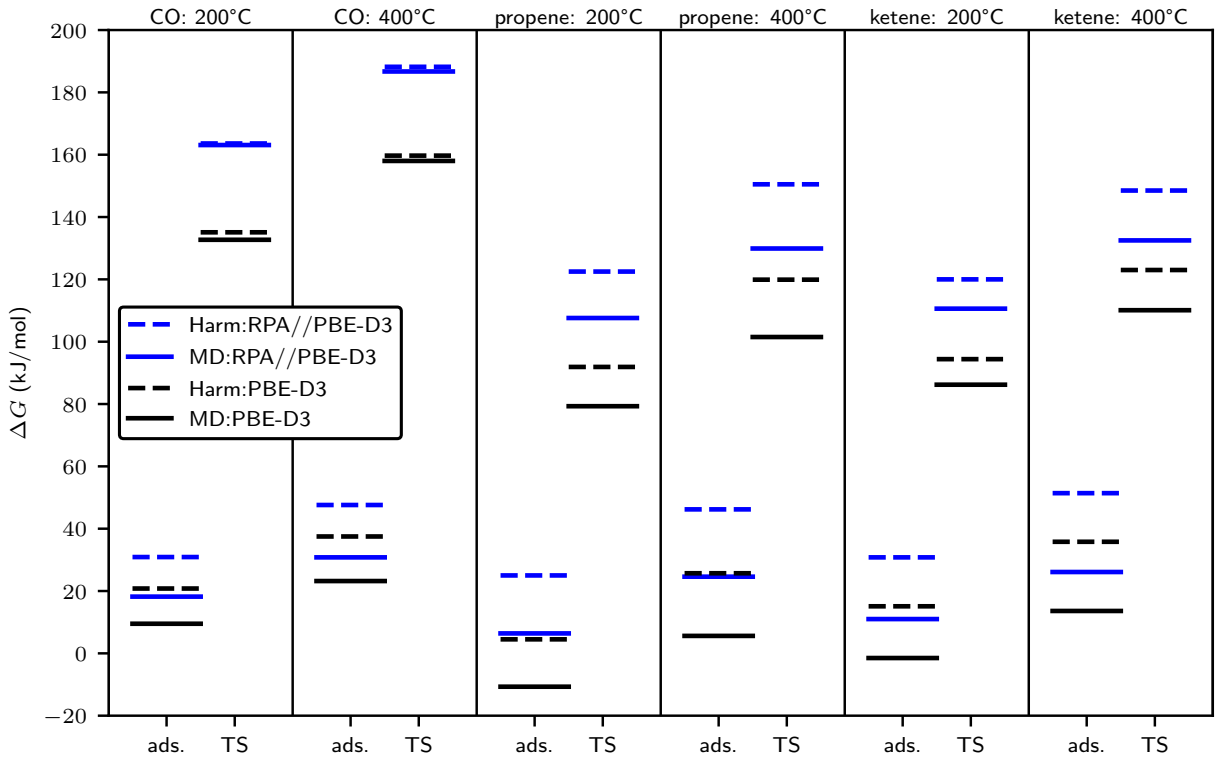

Figure 5: Summary of Gibbs free energies computed for adsorption of CO, propene and ketene at 200 °C and 400 °C and the respective transition state for methylation by an SMS. All free energies are referenced to the reactant in the gas phase at 1 bar reference pressure.

RPA-calculation using standard PAW potentials.

At this point, we will discuss the obtained adsorption and activation free energies and compare to the literature. We are not aware of experimental data for the adsorption at an SMS, however CO and propene have been studied for adsorption at Brønsted acid sites and in pristine zeolites. For CO, our best estimate for ΔG_{ads} is 18.2 and 30.8 kJ/mol at 200 °C and 400 °C, respectively (RPA with FEPT/MD in Table 4) . It is important to keep in mind that this refers to reference states of 1 bar in the gas phase and one molecule per unit cell in the adsorbed state. Adsorption experiments in zeolites are typically reported in terms of the uptake of molecules per mass of zeolite, in units of mol/kg or, equivalently, mmol/g. For comparison, an adsorption free energy of $\Delta G_{\mathrm{ads}} = 0$ at a partial pressure equal to the reference pressure, would result in a coverage of $\theta = 0.5$, which means for the T12 CHA unit cell studied here half a molecule per CHA cavity, corresponding to 0.7 mol/kg uptake. CO-adsorption is generally weak, which can already be concluded from the fact that IR-experiments on CO adsorbed at Brønsted acid sites are usually carried out at liquid nitrogen temperature to achieve sufficient coverage.[62] For H-MCM-22 and H-FER, coverages of the acid site of $\theta \approx 0.2$ were observed at about 30 °C and 0.225 bar partial pressure of CO.[63] For adsorption on isolated sites, based on the Langmuir adsorption isotherm, we deduce an experimental value of $\Delta G_{\mathrm{ads}} \approx$ -0.3 kJ/mol for these conditions. Given that fact that adsorption on an SMS is expected to be weaker than on a Brønsted acid site and that we study adsorption at much higher temperatures, we thus conclude that our values for ΔG_{ads} of CO fall in a reasonable range. For propylene, we find stronger adsorption than for CO, ΔG_{ads} is 6.4 and 24.6 kJ/mol at 200 °C and 400 °C (RPA with FEPT/MD in Table 4). The highest-temperature experimental adsorption measurement we found for propene reports an uptake of about 1.2 mol/kg at 1 bar and $T \approx 150$ °C in purely silicous CHA,[64] from which we deduce $\Delta G_{\mathrm{ads}} \approx$ -6.5 kJ/mol. Our value for ΔG_{ads} at 200 °C is thus 12.9 kJ/mol higher, which we consider to be in a reasonable range.

The adsorption and methylation of CO, propene and ketene is relevant in the MTO

process. Propene methylation is part of the olefin cycle and is a prototypical methylation reaction for terminal olefins heavier than ethene. The reactivity of CO and ketene within the MTO-process is discussed mainly as a likely initiation mechanism for the hydrocarbon pool,[65,66] when the first C-C bond is formed, but also in other areas.[67–80] Furthermore, CO-methylation is also the central step in the carbonylation of dimethyl ether.[81–83] Additionally, the reactivity of CO and ketene is important in the context of the methanol-to-syngas or OXZEO[84–86] (oxide-zeolite) processes, where a composite catalyst (reducible oxide and zeolite) transforms syngas (H_2+CO) directly to hydrocarbons.[87–90]

In our earliest work,[78,91] at 400 °C, we computed $\Delta G^{\ddagger}_{\text{app}} = 190$ kJ/mol for CO-methylation, 159 kJ/mol for ketene and 156 kJ/mol for propene using a correction based on MP2/def2-TZVPP calculations on cluster models. Using complete-basis-set (CBS)-extrapolated MP2 together with DLPNO-CCSD(T), we later obtained $\Delta G^{\ddagger}_{\text{app}} = 160$ kJ/mol for ketene, also at 400 °C.[80] While the barrier for CO-methylation is similar to our best RPA-estimate here (186.7 kJ/mol at 400 °C), the barriers for propene and ketene methylation are decidedly higher than the corresponding RPA-value obtained here (129.9 and 132.5 kJ/mol). This is due to both the anharmonicity (-18.4 and -12.8 kJ/mol for propene and ketene) as well as a higher barrier obtained already at the harmonic PBE-D3 level for the 36T-cell of chabazite, employing also lower precision and only a partial Hessian.[80]

Yang and coworkers obtained $\Delta A^{\ddagger}_{\text{int}} = 128$ kJ/mol for CO-methylation and $\Delta A^{\ddagger}_{\text{int}} = 78$ kJ/mol for ketene in H-SAPO-34 using metadynamics ($T = 670$ K) with revPBE-D3 and a double-zeta basis set.[89] The barrier for CO-methylation is similar to our PBE-D3 value of 134.8 kJ/mol at 400 °C (673.15 K), while our corresponding PBE-D3 barrier for ketene methylation is significantly higher (96.6 kJ/mol). The differences can be attributed to the different zeolite, different density functional and the definition of $\Delta A^{\ddagger}_{\text{int}}$, see Eq. 32. Using PBE-D2 and blue moon sampling, Bucko and coworkers computed activation barriers for side and main pocket of H-MOR ($T = 440$ K) of $\Delta A^{\ddagger}_{\text{int}} = 102$ and 130 kJ/mol, similar to our PBE-D3 value of 134.8 kJ/mol at 200 °C (473.15 K).

Summary and Conclusion

An approach has been proposed to compute anharmonic adsorption free energies based on DFT calculations. Similar, to the Widom test particle method,[41,42] the interaction between adsorbate and zeolite is computed by switching on or off the interaction between the two. This quantity can be computed with forward and backward free energy perturbation theory or the BAR method. Using an intermediate hard sphere model allows to greatly improve the overlap between the distributions of interacting and non-interacting states.

The main goal of obtaining accurate adsorption free energies from MD simulations was to be able to use these within the investigation of reaction mechanisms. A simple, yet relevant example has been investigated here, the methylation of different reactants by an SMS. In this case, coadsorption of the reactant with an SMS is generally weak and is then followed by a single transition state to yield the methylated product. The decisive quantity for reaction kinetics in this case is then the apparent activation free energy, which was determined here for CO, propene and ketene at temperatures of 200 °C and 400 °C.

For adsorption, the harmonic free energies are too weak by about 10 to 20 kJ/mol. This can be readily explained by the fact that the weakly adsorbed reactants can rotate and translate in the pore, which cannnot be described correctly the harmonic approximation. For apparent activation energies, anharmonicities are generally smaller than for the adsorbed reactants. For CO, the difference between MD and harmonic approximation is insignificant (< 3 kJ/mol). For ketene and propene, the anharmonicity of the apparent activation free energy is around 3 to 10 kJ/mol smaller then for the respective adsorption free energies, but overall in a similar range (10 to 20 kJ/mol).

To improve upon the limited accuracy of PBE-D3, RPA-calculations were performed, both as single points for the stationary points and using free energy perturbation theory (FEPT) for the MD simulations. One of the main results is that for the cases considered here, RPA-corrections to the PBE-D3 results agree very well, when computed with as a single point or with FEPT. Especially for apparent activation barriers, which are underestimated

by PBE-D3 by about 20 to 30 kJ/mol, the difference between single point and FEPT is only around 2 kJ/mol. Therefore, applying a correction based only on a single point would clearly be a significant improvement over a plain PBE-D3 calculation.

In its present form, this method is not expected to work for strongly bound, localized adsorbates, which will not have enough overlap with the reference state in which the adsorbate behaves as an ideal gas. Strongly bound adsorbates could be treated with this approach when they are first forced to desorb from the active site into the pore using a constraint or a bias potential. The free energy for desorption into the pore has been computed in this way for NH_3 in Cu-SSZ-13.[92] Another technical limitation is that RPA-calculations are applicable only to small unit cells, although extension to larger systems is possible using machine learning.[27,28] Besides technical limitations, it is also noteworthy that real catalyst may differ from the idealized isolated Brønsted acid site model and may feature also proximate Brønsted acid sites[93–97] or Lewis acid sites, either as extra-framework[98–104] or surface sites.[43,105–108] Furthermore, the rate of catalytic reactions in zeolite also depends on diffusion phenomena and can be influenced by co-adsorbates.[109–111]

Acknowledgement

I thank Tomáš Bučko for helpful discussions. The author acknowledges support by the state of Baden-Württemberg through bwHPC (bwunicluster and JUSTUS, RV bw17D011) and the German Research Foundation (DFG) through grant no INST 40/575-1 FUGG (JUSTUS 2 cluster). Financial support from the Helmholtz Association is also gratefully acknowledged. Gefördert durch die Deutsche Forschungsgemeinschaft (DFG) Projektnummer 434253773.

Supporting Information Available

Supporting Information: Additional analysis for different hard-sphere radii and raw data such as total energies and Cartesian coordinates of stationary points. MD trajectories are

supplied in a repository.[112]

References

(1) Stöcker, M. Methanol-to-hydrocarbons: catalytic materials and their behavior. *Microporous Mesoporous Mater.* **1999**, *29*, 3–48.

(2) Olsbye, U.; Svelle, S.; Bjorgen, M.; Beato, P.; Janssens, T. V.; Joensen, F.; Bordiga, S.; Lillerud, K. P. Conversion of methanol to hydrocarbons: how zeolite cavity and pore size controls product selectivity. *Angew. Chem. Int. Ed. Engl.* **2012**, *51*, 5810–31.

(3) Olah, G. A. Beyond oil and gas: the methanol economy. *Angew. Chem. Int. Ed. Engl.* **2005**, *44*, 2636–9.

(4) Olah, G. A. Towards oil independence through renewable methanol chemistry. *Angew. Chem. Int. Ed. Engl.* **2013**, *52*, 104–7.

(5) Yarulina, I.; Chowdhury, A. D.; Meirer, F.; Weckhuysen, B. M.; Gascon, J. Recent trends and fundamental insights in the methanol-to-hydrocarbons process. *Nat. Catal.* **2018**, *1*, 398–411.

(6) Van Speybroeck, V.; De Wispelaere, K.; Van der Mynsbrugge, J.; Vandichel, M.; Hemelsoet, K.; Waroquier, M. First principle chemical kinetics in zeolites: the methanol-to-olefin process as a case study. *Chem. Soc. Rev.* **2014**, *43*, 7326–57.

(7) Van Speybroeck, V.; Hemelsoet, K.; Joos, L.; Waroquier, M.; Bell, R. G.; Catlow, C. R. Advances in theory and their application within the field of zeolite chemistry. *Chem. Soc. Rev.* **2015**, *44*, 7044–111.

(8) Chizallet, C.; Bouchy, C.; Larmier, K.; Pirngruber, G. Molecular Views on Mechanisms of Bronsted Acid-Catalyzed Reactions in Zeolites. *Chem Rev* **2023**, *123*, 6107–6196.

(9) Rey, J.; Gomez, A.; Raybaud, P.; Chizallet, C.; Bučko, T. On the origin of the difference between type A and type B skeletal isomerization of alkenes catalyzed by zeolites: The crucial input of ab initio molecular dynamics. *J. Catal.* **2019**, *373*, 361–373.

(10) Piccini, G.; Alessio, M.; Sauer, J.; Zhi, Y.; Liu, Y.; Kolvenbach, R.; Jentys, A.; Lercher, J. A. Accurate Adsorption Thermodynamics of Small Alkanes in Zeolites. Ab initio Theory and Experiment for H-Chabazite. *J. Phys. Chem. C* **2015**, *119*, 6128–6137.

(11) Piccini, G.; Alessio, M.; Sauer, J. Ab initio study of methanol and ethanol adsorption on Bronsted sites in zeolite H-MFI. *Phys. Chem. Chem. Phys.* **2018**, *20*, 19964–19970.

(12) Rybicki, M.; Sauer, J. Ab Initio Prediction of Proton Exchange Barriers for Alkanes at Bronsted Sites of Zeolite H-MFI. *J. Am. Chem. Soc.* **2018**, *140*, 18151–18161.

(13) Sauer, J. Ab Initio Calculations for Molecule-Surface Interactions with Chemical Accuracy. *Acc. Chem. Res.* **2019**, *52*, 3502–3510.

(14) Ren, Q.; Rybicki, M.; Sauer, J. Interaction of C3–C5 Alkenes with Zeolitic Brønsted Sites: π-Complexes, Alkoxides, and Carbenium Ions in H-FER. *J. Phys. Chem. C* **2020**, *124*, 10067–10078.

(15) Van Speybroeck, V.; Bocus, M.; Cnudde, P.; Vanduyfhuys, L. Operando Modeling of Zeolite-Catalyzed Reactions Using First-Principles Molecular Dynamics Simulations. *ACS Catal.* **2023**, *13*, 11455–11493.

(16) Perdew, J. P.; Burke, K.; Ernzerhof, M. Generalized Gradient Approximation Made Simple. *Phys. Rev. Lett.* **1996**, *77*, 3865–3868.

(17) Grimme, S.; Antony, J.; Ehrlich, S.; Krieg, H. A Consistent and Accurate Ab Initio Parametrization of Density Functional Dispersion Correction (DFT-D) for the 94 Elements H-Pu. *J. Chem. Phys.* **2010**, *132*, 154104.

(18) Grimme, S. Semiempirical GGA-type density functional constructed with a long-range dispersion correction. *J. Comput. Chem.* **2006**, *27*, 1787–99.

(19) De Wispelaere, K.; Plessow, P. N.; Studt, F. Toward Computing Accurate Free Energies in Heterogeneous Catalysis: a Case Study for Adsorbed Isobutene in H-ZSM-5. *ACS Physical Chemistry Au* **2022**, *2*, 399–406.

(20) Zwanzig, R. W. High-Temperature Equation of State by a Perturbation Method. I. Nonpolar Gases. *J. Chem. Phys.* **1954**, *22*, 1420–1426.

(21) Bohm, D.; Pines, D. A Collective Description of Electron Interactions. I. Magnetic Interactions. *Phys. Rev.* **1951**, *82*, 625–634.

(22) Furche, F. Molecular tests of the random phase approximation to the exchange-correlation energy functional. *Phys. Rev. B* **2001**, *64*.

(23) Harl, J.; Kresse, G. Accurate Bulk Properties from Approximate Many-Body Techniques. *Phys. Rev. Lett.* **2009**, *103*, 056401.

(24) Göltl, F.; Gruneis, A.; Bucko, T.; Hafner, J. Van der Waals interactions between hydrocarbon molecules and zeolites: periodic calculations at different levels of theory, from density functional theory to the random phase approximation and Moller-Plesset perturbation theory. *J. Chem. Phys.* **2012**, *137*, 114111.

(25) Klimes, J.; Tew, D. P. Efficient and accurate description of adsorption in zeolites. *J. Chem. Phys.* **2019**, *151*, 234108.

(26) Rey, J.; Chizallet, C.; Rocca, D.; Bucko, T.; Badawi, M. Reference-Quality Free Energy Barriers in Catalysis from Machine Learning Thermodynamic Perturbation Theory. *Angew. Chem. Int. Ed. Engl.* **2024**, *63*, e202312392.

(27) Chehaibou, B.; Badawi, M.; Bucko, T.; Bazhirov, T.; Rocca, D. Computing RPA

Adsorption Enthalpies by Machine Learning Thermodynamic Perturbation Theory. *J. Chem. Theory Comput.* **2019**, *15*, 6333–6342.

(28) Bocus, M.; Vandenhaute, S.; Van Speybroeck, V. The Operando Nature of Isobutene Adsorbed in Zeolite H-SSZ-13 Unraveled by Machine Learning Potentials Beyond DFT Accuracy. *Angew. Chem. Int. Ed. Engl.* **2024**, e202413637.

(29) Laio, A.; Parrinello, M. Escaping free-energy minima. *Proc. Natl. Acad. Sci. U. S. A.* **2002**, *99*, 12562–6.

(30) Torrie, G. M.; Valleau, J. P. Nonphysical sampling distributions in Monte Carlo free-energy estimation: Umbrella sampling. *J. Comp. Phys.* **1977**, *23*, 187–199.

(31) Kästner, J. Umbrella sampling. *Wiley Interdiscip. Rev. Comput. Mol. Sci.* **2011**, *1*, 932–942.

(32) Kastner, J.; Thiel, W. Bridging the gap between thermodynamic integration and umbrella sampling provides a novel analysis method: "Umbrella integration". *J. Chem. Phys.* **2005**, *123*, 144104.

(33) Carter, E. A.; Ciccotti, G.; Hynes, J. T.; Kapral, R. Constrained Reaction Coordinate Dynamics for the Simulation of Rare Events. *Chem. Phys. Lett.* **1989**, *156*, 472–477.

(34) Sprik, M.; Ciccotti, G. Free energy from constrained molecular dynamics. *J. Chem. Phys.* **1998**, *109*, 7737–7744.

(35) Kozuch, S.; Shaik, S. How to conceptualize catalytic cycles? The energetic span model. *Acc. Chem. Res.* **2011**, *44*, 101–10.

(36) Jørgensen, M.; Chen, L.; Grönbeck, H. Monte Carlo Potential Energy Sampling for Molecular Entropy in Zeolites. *J. Phys. Chem. C* **2018**, *122*, 20351–20357.

(37) Amsler, J.; Plessow, P. N.; Studt, F.; Bucko, T. Anharmonic Correction to Adsorption Free Energy from DFT-Based MD Using Thermodynamic Integration. *J. Chem. Theory Comput.* **2021**, *17*, 1155–1169.

(38) Amsler, J.; Plessow, P. N.; Studt, F.; Bucko, T. Anharmonic Correction to Free Energy Barriers from DFT-Based Molecular Dynamics Using Constrained Thermodynamic Integration. *J. Chem. Theory Comput.* **2023**, *19*, 2455–2468.

(39) Chipot, C.; Pohorille, A. *Free energy calculations*; Springer, 2007; Vol. 86.

(40) Konig, G.; Bruckner, S.; Boresch, S. Unorthodox uses of Bennett's acceptance ratio method. *J. Comput. Chem.* **2009**, *30*, 1712–8.

(41) Widom, B. Some Topics in the Theory of Fluids. *J. Chem. Phys.* **1963**, *39*, 2808–2812.

(42) Widom, B. Potential-Distribution Theory and the Statistical Mechanics of Flulds. *J. Phys. Chem.* **1982**, *86*, 869–872.

(43) Smit, B.; Maesen, T. L. Molecular simulations of zeolites: adsorption, diffusion, and shape selectivity. *Chem Rev* **2008**, *108*, 4125–84.

(44) Ravichandran, S.; Najafi, M.; Goeminne, R.; Denayer, J. F. M.; Van Speybroeck, V.; Vanduyfhuys, L. Reaching Quantum Accuracy in Predicting Adsorption Properties for Ethane/Ethene in Zeolitic Imidazolate Framework-8 at Low Pressure Regime. *J. Chem. Theory Comput.* **2024**, *20*, 5225–5240.

(45) Vandenbrande, S.; Verstraelen, T.; Gutierrez-Sevillano, J. J.; Waroquier, M.; Van Speybroeck, V. Methane Adsorption in Zr-Based MOFs: Comparison and Critical Evaluation of Force Fields. *J Phys Chem C Nanomater Interfaces* **2017**, *121*, 25309–25322.

(46) Lee, Y.; Poloni, R.; Kim, J. Probing gas adsorption in MOFs using an efficient ab initio widom insertion Monte Carlo method. *J. Comput. Chem.* **2016**, *37*, 2808–2815.

(47) Goeminne, R.; Van Speybroeck, V. Ab Initio Predictions of Adsorption in Flexible Metal-Organic Frameworks for Water Harvesting Applications. *J. Am. Chem. Soc.* **2025**, *147*, 3615–3630.

(48) Kresse, G.; Furthmuller, J. Efficient Iterative Schemes for Ab Initio Total-Energy Calculations using a Plane-Wave Basis Set. *Phys. Rev. B* **1996**, *54*, 11169–11186.

(49) Kresse, G.; Joubert, D. From Ultrasoft Pseudopotentials to the Projector Augmented-Wave Method. *Phys. Rev. B* **1999**, *59*, 1758–1775.

(50) Tuckerman, M. E. *Statistical mechanics: theory and molecular simulation*; Oxford university press, 2023.

(51) Schiferl, S. K.; Wallace, D. C. Statistical errors in molecular dynamics averages. *J. Chem. Phys.* **1985**, *83*, 5203–5209.

(52) Flyvbjerg, H.; Petersen, H. G. Error estimates on averages of correlated data. *J. Chem. Phys.* **1989**, *91*, 461–466.

(53) Kaltak, M.; Klimes, J.; Kresse, G. Cubic scaling algorithm for the random phase approximation: Self-interstitials and vacancies in Si. *Phys. Rev. B* **2014**, *90*.

(54) Bennett, C. H. Efficient estimation of free energy differences from Monte Carlo data. *J. Comp. Phys.* **1976**, *22*, 245–268.

(55) Pohorille, A.; Jarzynski, C.; Chipot, C. Good practices in free-energy calculations. *J. Phys. Chem. B* **2010**, *114*, 10235–53.

(56) Gomes, J.; Head-Gordon, M.; Bell, A. T. Reaction Dynamics of Zeolite-Catalyzed Alkene Methylation by Methanol. *J. Phys. Chem. C* **2014**, *118*, 21409–21419.

(57) Ryckaert, J.-P.; Ciccotti, G.; Berendsen, H. J. C. Numerical integration of the cartesian equations of motion of a system with constraints: molecular dynamics of n-alkanes. *J. Comp. Phys.* **1977**, *23*, 327–341.

(58) Bucko, T.; Chibani, S.; Paul, J. F.; Cantrel, L.; Badawi, M. Dissociative iodomethane adsorption on Ag-MOR and the formation of AgI clusters: an ab initio molecular dynamics study. *Phys. Chem. Chem. Phys.* **2017**, *19*, 27530–27543.

(59) Zheng, J.; Truhlar, D. G. Multi-path variational transition state theory for chemical reaction rates of complex polyatomic species: ethanol + OH reactions. *Faraday Discuss.* **2012**, *157*, 59–88; discussion 113–40.

(60) Bucko, T.; Gesvandtnerova, M.; Rocca, D. Ab Initio Calculations of Free Energy of Activation at Multiple Electronic Structure Levels Made Affordable: An Effective Combination of Perturbation Theory and Machine Learning. *J. Chem. Theory Comput.* **2020**, *16*, 6049–6060.

(61) Huber, P.; Plessow, P. N. Accurate and Efficient Description of Acidic Zeolites with Plane-Wave Density Functional Theory Using Range-Separated Hybrid Functionals. *ChemPhysChem* **2025**, e2500147.

(62) Zecchina, A.; Arean, C. O. Diatomic molecular probes for mid-IR studies of zeolites. *Chem. Soc. Rev.* **1996**, *25*, 187–+.

(63) Arean, C. O.; Delgado, M. R.; Nachtigall, P.; Thang, H. V.; Rubes, M.; Bulanek, R.; Chlubna-Eliasova, P. Measuring the Bronsted acid strength of zeolites–does it correlate with the O-H frequency shift probed by a weak base? *Phys. Chem. Chem. Phys.* **2014**, *16*, 10129–41.

(64) Maghsoudi, H.; Abdi, H.; Aidani, A. Temperature- and Pressure-Dependent Adsorption Equilibria and Diffusivities of Propylene and Propane in Pure-Silica Si-CHA Zeolite. *Ind. Eng. Chem. Res.* **2020**, *59*, 1682–1692.

(65) Dahl, I. M.; Kolboe, S. On the Reaction Mechanism for Hydrocarbon Formation from Methanol over SAPO-34: I. Isotopic Labeling Studies of the Co-Reaction of Ethene and Methanol. *J. Catal.* **1994**, *149*, 458–464.

(66) Dahl, I. M.; Kolboe, S. On the reaction mechanism for hydrocarbon formation from methanol over SAPO-34 .2. Isotopic labeling studies of the co-reaction of propene and methanol. *J. Catal.* **1996**, *161*, 304–309.

(67) Chowdhury, A. D.; Houben, K.; Whiting, G. T.; Mokhtar, M.; Asiri, A. M.; Al-Thabaiti, S. A.; Basahel, S. N.; Baldus, M.; Weckhuysen, B. M. Initial Carbon-Carbon Bond Formation during the Early Stages of the Methanol-to-Olefin Process Proven by Zeolite-Trapped Acetate and Methyl Acetate. *Angew. Chem. Int. Ed. Engl.* **2016**, *55*, 15840–15845.

(68) Chowdhury, A. D.; Gascon, J. The Curious Case of Ketene in Zeolite Chemistry and Catalysis. *Angew. Chem. Int. Ed. Engl.* **2018**, *57*, 14982–14985.

(69) Chowdhury, A. D.; Paioni, A. L.; Houben, K.; Whiting, G. T.; Baldus, M.; Weckhuysen, B. M. Bridging the Gap between the Direct and Hydrocarbon Pool Mechanisms of the Methanol-to-Hydrocarbons Process. *Angew. Chem. Int. Ed. Engl.* **2018**, *57*, 8095–8099.

(70) Gong, X.; Caglayan, M.; Ye, Y.; Liu, K.; Gascon, J.; Dutta Chowdhury, A. First-Generation Organic Reaction Intermediates in Zeolite Chemistry and Catalysis. *Chem Rev* **2022**, *122*, 14275–14345.

(71) Liu, Y.; Muller, S.; Berger, D.; Jelic, J.; Reuter, K.; Tonigold, M.; Sanchez-Sanchez, M.; Lercher, J. A. Formation Mechanism of the First Carbon-Carbon Bond and the First Olefin in the Methanol Conversion into Hydrocarbons. *Angew. Chem. Int. Ed. Engl.* **2016**, *55*, 5723–6.

(72) Tajima, N.; Tsuneda, T.; Toyama, F.; Hirao, K. A New Mechanism for the First Carbon-Carbon Bond Formation in the MTG Process: A Theoretical Study. *J. Am. Chem. Soc.* **1998**, *120*, 8222–8229.

(73) Hutchings, G. J.; Hunter, R.; Johnston, P.; Vanrensburg, L. J. Methanol Conversion to Hydrocarbons over Zeolite H-ZSM-5: Investigation of the Role of CO and Ketene in the Formation of the Initial C-C Bond. *J. Catal.* **1993**, *142*, 602–616.

(74) Hutchings, G. J.; Gottschalk, F.; Hall, M. V. M.; Hunter, R. Hydrocarbon Formation from Methylating Agents over the Zeolite Catalyst Zsm-5 - Comments on the Mechanism of Carbon Carbon Bond and Methane Formation. *J. Chem. Soc., Faraday Trans.* **1987**, *83*, 571–583.

(75) Song, W.; Marcus, D. M.; Fu, H.; Ehresmann, J. O.; Haw, J. F. An Oft-Studied Reaction That May Never Have Been: Direct Catalytic Conversion of Methanol or Dimethyl Ether to Hydrocarbons on the Solid Acids HZSM-5 or HSAPO-34. *J. Am. Chem. Soc.* **2002**, *124*.

(76) Guo, Z.; Chen, Q.; Liu, J.; Yang, B. Discovery of ketene/acetyl as a potential receptor for hydrogen-transfer reactions in zeolites. *Nat. Commun.* **2025**, *16*, 1152.

(77) Wu, X.; Zhang, Z.; Pan, Z.; Zhou, X.; Bodi, A.; Hemberger, P. Ketenes in the Induction of the Methanol-to-Olefins Process. *Angew. Chem. Int. Ed. Engl.* **2022**, *61*, e202207777.

(78) Plessow, P. N.; Studt, F. Unraveling the Mechanism of the Initiation Reaction of the Methanol to Olefins Process Using ab Initio and DFT Calculations. *ACS Catal.* **2017**, *7*, 7987–7994.

(79) Huber, P.; Plessow, P. N. A computational investigation of the decomposition of acetic acid in H-SSZ-13 and its role in the initiation of the MTO process. *Catal. Sci. Technol.* **2023**, *13*, 1905–1917.

(80) Huber, P.; Plessow, P. N. The role of decarboxylation reactions during the initiation of the methanol-to-olefins process. *J. Catal.* **2023**, *428*.

(81) Cheung, P.; Bhan, A.; Sunley, G. J.; Iglesia, E. Selective carbonylation of dimethyl ether to methyl acetate catalyzed by acidic zeolites. *Angew. Chem. Int. Ed. Engl.* **2006**, *45*, 1617–20.

(82) Boronat, M.; Martinez-Sanchez, C.; Law, D.; Corma, A. Enzyme-like specificity in zeolites: a unique site position in mordenite for selective carbonylation of methanol and dimethyl ether with CO. *J. Am. Chem. Soc.* **2008**, *130*, 16316–23.

(83) Xiong, D.; Lai, Z.; Chen, J.; Yuan, H.; Wang, H. Ketene Conversion Chemistry within Mordenite Zeolite: Pore-Size-Dependent Reaction Mechanism, Product Selectivity, and Catalytic Activity. *J. Am. Chem. Soc.* **2025**, *147*, 17303–17314.

(84) Jiao, F. et al. Selective conversion of syngas to light olefins. *Science* **2016**, *351*, 1065–8.

(85) Ji, Y.; Gao, P.; Zhao, Z.; Xiao, D.; Han, Q.; Chen, H.; Gong, K.; Chen, K.; Han, X.; Bao, X.; Hou, G. Oxygenate-based routes regulate syngas conversion over oxide–zeolite bifunctional catalysts. *Nat. Catal.* **2022**, *5*, 594–604.

(86) Zhang, Y.; Gao, P.; Jiao, F.; Chen, Y.; Ding, Y.; Hou, G.; Pan, X.; Bao, X. Chemistry of Ketene Transformation to Gasoline Catalyzed by H-SAPO-11. *J. Am. Chem. Soc.* **2022**, *144*, 18251–18258.

(87) Wang, C. M.; Wang, Y. D.; Xie, Z. K. Methylation of olefins with ketene in zeotypes and its implications for the direct conversion of syngas to light olefins: a periodic DFT study. *Catal. Sci. Technol.* **2016**, *6*, 6644–6649.

(88) Ke, J.; Wang, Y.-D.; Wang, C.-M.; Xie, Z.-K. Microkinetic simulations of ketene conversion to olefins in H-SAPO-34 zeolite for bifunctional catalysis. *Catal. Sci. Technol.* **2024**, *14*, 3728–3738.

(89) Chen, Q.; Liu, J.; Yang, B. Resolving the Relations between Methanol and

Ketene/Acetyl within HSAPO-34 in the Bifunctional Syngas-to-Olefin Process. *ACS Catal.* **2025**, *15*, 10796–10807.

(90) Chen, W.; Li, G.; Yi, X.; Day, S. J.; Tarach, K. A.; Liu, Z.; Liu, S. B.; Edman Tsang, S. C.; Gora-Marek, K.; Zheng, A. Molecular Understanding of the Catalytic Consequence of Ketene Intermediates under Confinement. *J. Am. Chem. Soc.* **2021**, *143*, 15440–15452.

(91) Plessow, P. N.; Smith, A.; Tischer, S.; Studt, F. Identification of the Reaction Sequence of the MTO Initiation Mechanism Using Ab Initio-Based Kinetics. *J. Am. Chem. Soc.* **2019**, *141*, 5908–5915.

(92) Li, H.; Paolucci, C.; Schneider, W. F. Zeolite Adsorption Free Energies from ab Initio Potentials of Mean Force. *J. Chem. Theory Comput.* **2018**, *14*, 929–938.

(93) Nystrom, S.; Hoffman, A.; Hibbitts, D. Tuning Brønsted Acid Strength by Altering Site Proximity in CHA Framework Zeolites. *ACS Catal.* **2018**, *8*, 7842–7860.

(94) Di Iorio, J. R.; Hoffman, A. J.; Nimlos, C. T.; Nystrom, S.; Hibbitts, D.; Gounder, R. Mechanistic origins of the high-pressure inhibition of methanol dehydration rates in small-pore acidic zeolites. *J. Catal.* **2019**, *380*, 161–177.

(95) Hoffman, A. J.; Bates, J. S.; Di Iorio, J. R.; Nystrom, S. V.; Nimlos, C. T.; Gounder, R.; Hibbitts, D. Rigid Arrangements of Ionic Charge in Zeolite Frameworks Conferred by Specific Aluminum Distributions Preferentially Stabilize Alkanol Dehydration Transition States. *Angew. Chem. Int. Ed. Engl.* **2020**, *59*, 18686–18694.

(96) Smith, A. T.; Plessow, P. N.; Studt, F. Trends in the Reactivity of Proximate Aluminum Sites in H-SSZ-13. *J. Phys. Chem. C* **2021**, *125*, 16508–16515.

(97) Plessow, P. N.; Studt, F. Cooperative Effects of Active Sites in the MTO Process:

A Computational Study of the Aromatic Cycle in H-SSZ-13. *ACS Catal.* **2022**, *13*, 624–632.

(98) Khramenkova, E. V.; Venkatraman, H.; Soethout, V.; Pidko, E. A. Global optimization of extraframework ensembles in zeolites: structural analysis of extraframework aluminum species in MOR and MFI zeolites. *Phys. Chem. Chem. Phys.* **2022**, *24*, 27047–27054.

(99) Liu, C.; Li, G.; Hensen, E. J. M.; Pidko, E. A. Nature and Catalytic Role of Extraframework Aluminum in Faujasite Zeolite: A Theoretical Perspective. *ACS Catal.* **2015**, *5*, 7024–7033.

(100) Yi, X.; Liu, K.; Chen, W.; Li, J.; Xu, S.; Li, C.; Xiao, Y.; Liu, H.; Guo, X.; Liu, S. B.; Zheng, A. Origin and Structural Characteristics of Tri-coordinated Extra-framework Aluminum Species in Dealuminated Zeolites. *J. Am. Chem. Soc.* **2018**, *140*, 10764–10774.

(101) Ravi, M.; Sushkevich, V. L.; van Bokhoven, J. A. Towards a better understanding of Lewis acidic aluminium in zeolites. *Nat. Mater.* **2020**, *19*, 1047–1056.

(102) Yakimov, A. V.; Ravi, M.; Verel, R.; Sushkevich, V. L.; van Bokhoven, J. A.; Copéret, C. Structure and Framework Association of Lewis Acid Sites in MOR Zeolite. *J. Am. Chem. Soc.* **2022**, *144*, 10377–10385.

(103) Jin, M.; Ravi, M.; Lei, C.; Heard, C. J.; Brivio, F.; Tosner, Z.; Grajciar, L.; van Bokhoven, J. A.; Nachtigall, P. Dynamical Equilibrium between Bronsted and Lewis Sites in Zeolites: Framework-Associated Octahedral Aluminum. *Angew. Chem. Int. Ed. Engl.* **2023**, *62*, e202306183.

(104) Mancuso, J. L.; Van Speybroeck, V. The nature of extraframework aluminum species and Brønsted acid site interactions under catalytic operating conditions. *J. Catal.* **2024**, *429*.

(105) Rey, J.; Raybaud, P.; Chizallet, C. Ab Initio Simulation of the Acid Sites at the External Surface of Zeolite Beta. *ChemCatChem* **2017**, *9*, 2176–2185.

(106) Cnudde, P.; Demuynck, R.; Vandenbrande, S.; Waroquier, M.; Sastre, G.; Speybroeck, V. V. Light Olefin Diffusion during the MTO Process on H-SAPO-34: A Complex Interplay of Molecular Factors. *J. Am. Chem. Soc.* **2020**, *142*, 6007–6017.

(107) Treps, L.; Gomez, A.; Bruin, T. d.; Chizallet, C. Environment, Stability and Acidity of External Surface Sites of Silicalite-1 and ZSM-5 Micro and Nano Slabs, Sheets, and Crystals. *ACS Catal.* **2020**, *10*, 3297–3312.

(108) Huber, P.; Studt, F.; Plessow, P. N. Reactivity of Surface Lewis and Brønsted Acid Sites in Zeolite Catalysis: A Computational Case Study of DME Synthesis Using H-SSZ-13. *J. Phys. Chem. C* **2022**, *126*, 5896–5905.

(109) De Wispelaere, K.; Wondergem, C. S.; Ensing, B.; Hemelsoet, K.; Meijer, E. J.; Weckhuysen, B. M.; Van Speybroeck, V.; Ruiz-Martinez, J. Insight into the Effect of Water on the Methanol-to-Olefins Conversion in H-SAPO-34 from Molecular Simulations and in Situ Microspectroscopy. *ACS Catal.* **2016**, *6*, 1991–2002.

(110) DeLuca, M.; Hibbitts, D. Predicting diffusion barriers and diffusivities of C6–C12 methylbenzenes in MFI zeolites. *Microporous Mesoporous Mater.* **2022**, *333*.

(111) Cnudde, P.; Redekop, E. A.; Dai, W.; Porcaro, N. G.; Waroquier, M.; Bordiga, S.; Hunger, M.; Li, L.; Olsbye, U.; Van Speybroeck, V. Experimental and Theoretical Evidence for the Promotional Effect of Acid Sites on the Diffusion of Alkenes through Small-Pore Zeolites. *Angew. Chem. Int. Ed. Engl.* **2021**, *60*, 10016–10022.

(112) Plessow, P. N. **2025**, DOI 10.35097/y316cba2b66vncwk.

TOC Graphic

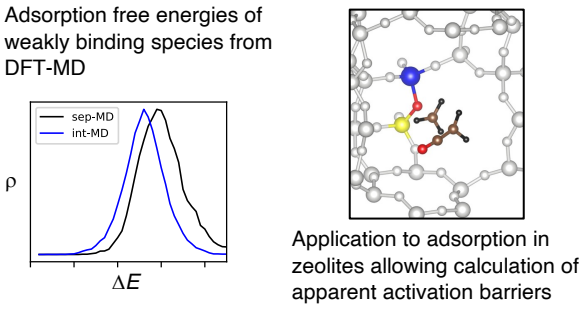

Figure 6: TOC Graphic